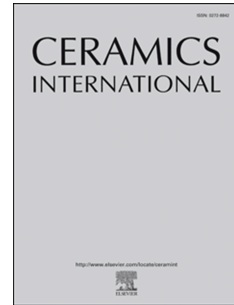# Journal Pre-proof

Innovative improvement of sintered ceramic electrolytes by salt infiltration

João P.F. Grilo, Daniel A. Macedo, Rubens M. Nascimento, Fernando M.B. Marques

Innovative improvement of sintered ceramic electrolytes by salt infiltration

João P. F. Grilo[a, *], Daniel A. Macedo[b], Rubens M. Nascimento[c],

Fernando M. B. Marques[a, b, *, **]

[a] Department of Materials and Ceramic Engineering, CICECO – Aveiro Institute of Materials, University of Aveiro, 3810-193 Aveiro, Portugal

[b] Materials Science and Engineering Postgraduate Program, UFPB, 58051-900 João Pessoa, Brazil

[c] Materials Science and Engineering Postgraduate Program, UFRN, 59072-970 Natal, Brazil

Abstract

Previously sintered (1500 °C, 4 h) dense pellets of $Ce_{0.9}Gd_{0.1}O_{1.95}$ (GDC) were covered and heat treated with eutectic mixtures of Na_2CO_3 and Li_2CO_3 (NLC), and their electrical performance was assessed against pure GDC and chemically synthesized GDC+NLC. Microstructural analysis of NLC impregnated samples confirmed slight migration of the molten phase to the interior of the GDC pellets via grain boundaries, resulting in a significant improvement of the grain boundary conductivity, increasing with duration of heat treatment (0.5-2 h) and temperature (600 to 800 ºC range). The observed total conductivity exceeded in almost 20% the corresponding values obtained for standard GDC samples. Cells tested before and after direct current polarization (0.5 V, 500 °C) showed the same electrical performance, discarding the possibility of parallel contributions of salt ions to the total conductivity. Grain boundary engineering using salt infiltration is an effective tool to improve the electrical performance of ceramic electrolytes.

Keywords: Gd-doped ceria; molten carbonates; grain boundary; impedance spectroscopy.

*Corresponding author:

JPF Grilo – grilo.jpf@ua.pt

FMB Marques – fmarques@ua.pt

**Visiting Professor at (b)

1. Introduction

Ceria-based materials (usually GDC, Gd-doped ceria, or SDC, Sm-doped ceria) were extensively studied as potential electrolytes for Solid Oxide Fuel Cells (SOFCs) [1–4]. Sintering aids, mostly transition metal oxides and salts, may significantly decrease the usual sintering temperature of ceria-based electrolytes (often around 1500 °C). However, several sintering aids exhibit a negative influence on grain boundary conductivity, contributing to large ohmic losses at moderate temperatures [5–8]. Alkali metal salts (including eutectic mixtures) were also tested as sintering aids with ceria-based electrolytes. The efficacy concerning densification was clearly shown but only recently the electrical performance was considered in further detail [9–13].

Bulk and grain boundary conductivity enhancement claims (some of them remarkable, reaching two orders of magnitude) were reported for ceria-based electrolytes fired at low temperatures using Li salts as sintering aids [11,13]. However, these claims are not unanimous, with reports indicating negligible effects on bulk conductivity and even degradation of the grain boundary conductivity [10]. Distinct salts, various firing conditions and diversity of reference materials (from "homemade" to commercial) might explain the apparently disparate results.

Processing routes previously adopted involved joint firing of Li salts and ceramic precursors, a situation that could favor the partial dissolution of the sintering aid cation in the host lattice, given the size compatibility between host (Ce^{4+}) and foreign cation (Li^+). Furthermore, since typical Li salts (nitrates and carbonates) have low melting and decomposition temperatures, loss of Li to the gas phase is expected to occur even at modest sintering temperatures of only 1100 °C [11,14]. The uncertainty on the amount and local effects of alkali metal cations in the ceramic phase cannot be disclosed in such experiments. Na^+ ions, larger than Ce^{4+}, as such less likely to be dissolved in the lattice, would be a possible alternative to elucidate these issues. However, Na salts have higher melting and decomposition temperatures, performing poorly as sintering aids. In a known attempt following this approach, the amount of secondary phase (Na_2CO_3) exceeded by far the concept of sintering aid and the result was typical of a composite material [12].

Recently we have shown that small amounts of eutectic mixtures of alkali metal carbonates yield fully dense GDC samples at sintering temperatures up to 400 °C below those needed when conventional powders are used. The p-type conductivity of these materials was slightly lower when compared with standard GDC [15] and the grain boundary conductivity could be significantly improved in materials prepared by a chemical synthesis route [16]. However, the adopted processing routes, with all cations intimately mixed before sintering, also prevented the separate analysis of the interaction of alkali metal salts in the grain boundary region only.

2

This work exploits for the first time the impact of a eutectic salt mixture on the microstructure and electrical properties of previously sintered and dense GDC pellets, targeting grain boundary effects only. Grain boundaries are disordered regions in a polycrystal and often easy migration pathways for several species. This possibility was used already to change locally the grain boundary composition of dense electrolytes taking advantage of the enhanced diffusion rates (orders of magnitude higher) of some elements via grain boundaries with respect to bulk transport [17,18]. Since corrosion of dense ceramics by molten phases is also faster via grain boundaries [19], fully dense GDC pellets were fired at distinct temperatures and for different periods, top covered by a (molten) salt mixture. The impact of these heat treatments on dense GDC was assessed by impedance spectroscopy and complemented by microstructural observations. Only the grain boundary region was changed due to the moderate temperatures involved. Two additional sets of reference materials were included in this study to obtain further insight into observed effects. The first obvious reference was pure and dense GDC (commercial powder). The second reference material was dense GDC prepared with the same salt mixture as sintering aid, and prepared following a chemical route.

2. Experimental procedure

Na_2CO_3 and Li_2CO_3 (Sigma Aldrich, 99.9%) were mixed in the molar ratio of 48:52 to prepare the selected eutectic salt mixture (NLC). The reactants were mixed using high energy milling at 650 rpm for 30 min. GDC cylindrical pellets were prepared using a standard commercial powder, $Ce_{0.9}Gd_{0.1}O_{1.95}$ (Praxair). Disks were firstly shaped by uniaxial pressing and afterward isostatically pressed at 200 MPa and sintered at 1500 ℃ for 4 h. These samples were used as reference and for ulterior treatments with NLC.

NLC powder was uniaxially pressed into pellets and placed on the top of previously sintered GDC pellets. Such asymmetric double layer assemblies ($GDC_{bottom}|NLC_{top}$) were heat treated for 0.5, 1 and 2 h at 600-800 ℃ with a heating rate of 5 ℃/min. Since NLC was placed on the top of GDC pellets but the molten salt could flow freely above the eutectic temperature (500 °C), the top and side GDC surfaces were easily covered with NLC during these treatments. Only access of NLC to the GDC bottom surface (placed directly on an alumina holder) was partly constrained. Before all other tests (electrical measurements and microstructural analysis) the carbonate layer covering the GDC pellets was removed using a hydrochloric acid solution (1:3 acid:water ratio). A scheme of the process sequence is shown in Figure 1A. These cells will be named as GDC UT, 600, 700 and 800, meaning untreated (UT) or treated with an NLC layer

3

at 600, 700 and 800 ºC, respectively. When needed, the duration of the treatment (in h) is also included in the acronym (e.g., 800 2 for a 2 h treatment at 800 °C).
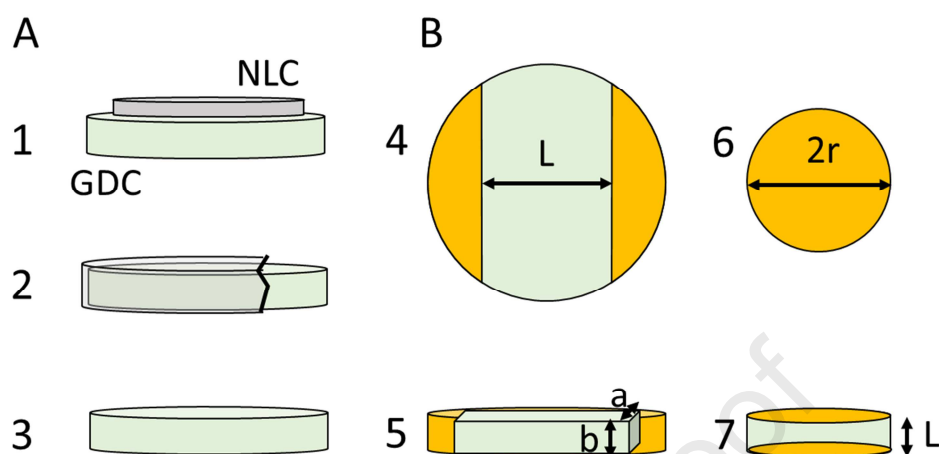

Figure 1. A - Scheme of NLC thermal treatments: (1) NLC pellets deposited on sintered GDC; (2) NLC layer covering the pellet after melting/heat treatment; (3) Clean GDC pellet after washing with diluted HCl; B - Schemes of electrode areas (yellow/dark grey) in the in-plane (4-5) and cross (6-7) arrangements. Top views (4&6) and assumed active cell volumes (5&7, green/light shadowed regions in between electrodes).

Pellets with 3 mol% NLC were also prepared by a chemical synthesis route (Pechini synthesis) where NLC is mixed with a precursor (resin) of the GDC powder [16,20] This precursor is the product of the reaction of citric acid and ethylene glycol, used as a chelating agent of dissolved Ce and Gd cations. Cerium and gadolinium nitrates in stoichiometric quantities are added to citric acid diluted in distilled water at ~ 65 °C, under constant stirring. After homogenization for 1 h, the precursor resin is formed with the addition of ethylene glycol at temperatures close to 80 °C. NLC is added directly to the resin. The resulting material is calcined in a furnace at 450 °C for 1 h. The calcined powder was disk-shaped (uniaxial pressing) and isostatically pressed at 200 MPa, before sintering at 1100 ºC for 4 h to reach full densification. The cell acronym (GDCNLC3S) prepared in this manner details the NLC content (3 mol%) and route (symbol S for chemical synthesis).

The electrical properties of all pellets were studied by impedance spectroscopy using porous Au electrodes (fired at 600 ºC for 20 min). Two distinct cell configurations were used, one involving in-plane electrodes (cells UT, 600, 700 and 800) covering circle segments in opposite sides of the pellets and separated by a distance much larger than the disk thickness (hereby called in-plane measurements). Some tests used also standard disk-shaped cells with electrodes deposited on opposite flat disk surfaces (Table 1, cells Cross and GDCNLC3S). The

4

latter tests will be hereby named as cross measurements. Schemes of these cells are presented in Figure 1B. All electrical measurements were performed in open air between 200 and 600 ℃ using an HP 4284A LCR Meter, with a signal amplitude of 0.5 and 1 V within the 20 Hz - 1 MHz frequency range. Direct current (dc) polarization experiments (total voltage of 0.5 V) were also performed at 500 °C, in air, to assess the possible role of salt ions on the electrical performance of selected cells. A short description of all samples studied in this work together with acronyms, compositions, processing routes and electrode configurations is presented in Table 1.

Table 1. Sample acronyms, compositions, processing routes and electrode configurations.

Acronym	Base pellet			NLC infiltration			Electrode configuration
	Route	Sintering T (°C)/t (h)	NLC content	Y/N	T (°C)	t (h)	
Cross	Ceramic	1500/4	-	No			Cross
UT	Ceramic	1500/4	-	No			In-plane
GDCNLC3S	Chemical	1100/4	3 mol%	No			Cross
600 1	Ceramic	1500/4	-	Yes	600	1	In-plane
700 1	Ceramic	1500/4	-	Yes	700	1	In-plane
800 0.5	Ceramic	1500/4	-	Yes	800	0.5	In-plane
800 1	Ceramic	1500/4	-	Yes	800	1	In-plane
800 2	Ceramic	1500/4	-	Yes	800	2	In-plane

Disks surfaces and fractured sections were used for microstructural characterization by scanning electron microscopy (SEM, Hitachi SU-70) coupled with energy dispersive X-ray analysis (EDS, Bruker Quantax 400). In some cases, thermal etching (15 min, 10% below the sintering temperature: 1350 ℃) of polished surfaces was used to highlight grain size. Attempts to use chemical etching instead of thermal etching had poor results. Some images were analyzed with Image J to measure the average area of grains (A), which was subsequently used to estimate a mean equivalent diameter $D = \sqrt{4A/\pi}$. Several samples were also studied by X-ray diffraction (XRD). Diffraction patterns (PANalytical, Xpert-pro diffractometer, CuKα radiation, 40 kV and 25 mA) were collected in the angular range of $20 \leq 2\theta \leq 80°$ (0.02°/step, 2 s/step). The MAUD (Materials Analyzing Using Diffraction) software package was used to determine the structural parameters.

3. Results and discussion

3.1 Structural and microstructural analysis

Pure GDC powder showed the standard fluorite structure pattern (28795 ICSD, Inorganic Crystal Structure Database). GDCNLC3S showed no vestige of any additional peaks

5

besides those characteristics of GDC. The lattice parameters of these powders were in close agreement (5.419(3) and 5.419(4) Å for GDC and GDCNLC3S, respectively). Samples treated with NLC were not studied by XRD. In fact, surface analysis (of pellets) would not be representative of the bulk and analysis of powdered samples would hardly show any trace of secondary phases, since their global amount is vestigial, as confirmed by SEM/EDS, situation detailed below.

Figure 2A shows the cross section of a pure GDC pellet after thermal etching. The corresponding cross sections of GDC infiltrated with NLC at 600 and 700 ºC for 1 h are shown in Figures 2B through 2E. Pictures in the left column were obtained close to the GDC bottom surface ("NLC free") while those in the right column were observed close to the attacked upper GDC surface. Dashed lines in bright regions indicate the approximate pellet outer surface plane (perpendicular to the observed cross section). All samples exhibit almost no porosity since highly densified GDC ceramics (> 95% theoretical density) were used in all tests.

Actual average grain sizes shown in Table 2 were obtained from lower magnification SEM pictures to increase the statistical quality of these data (see Supplementary Information, Figure S1). The grain size is similar in all cases (2.5 – 3 µm range) but with a slight tendency to increase with impregnation temperature and close to NLC covered surfaces (maximum of 3.1 µm for an NLC treatment at 800 °C, versus 2.4-2.6 µm for untreated GDC and all GDC bottom surfaces, almost NLC "free"). Thermal etching at high temperature (15 min) in the presence of (vestigial amounts of infiltrated) NLC was enough to promote slight grain growth. The only situation where the observed trend is not obeyed is on the grain size of top regions of GDC pellets that suffered chemical attack at 600 and 700 °C, where we can find an apparent slight reversal in grain growth. However, exact values are quite close (about 3.0 µm at 600 °C versus 2.8 µm at 700 °C) and this single apparent reversal of the general tendency can only be ascribed to scatter in experimental data.

Attempts to identify the presence of NLC in these materials involved EDS analysis in distinct sample locations, with the emphasis only on Ce, Gd and Na. Li is a light element outside the EDS analytical capabilities. Carbon was discarded since the sample preparation involved the deposition of C films before analysis. Typical results obtained by SEM/EDS are shown in Figure S2 (see Supplementary Information), including microstructure and atomic number maps for GDC 800 2 (top view) after removal of NLC with diluted HCl. The efficacy of salt removal with acid attack is easily confirmed by the clear observation of GDC grains at the free surface. There is no sign of secondary phases rich in alkali metal (Na) ions. The Na level, apparently uniform across the entire surface, might seem significant but the Na peak used for

EDS analysis is small and close to large Ce and Gd peaks. As such, Na easily appears as background level in similar analysis.
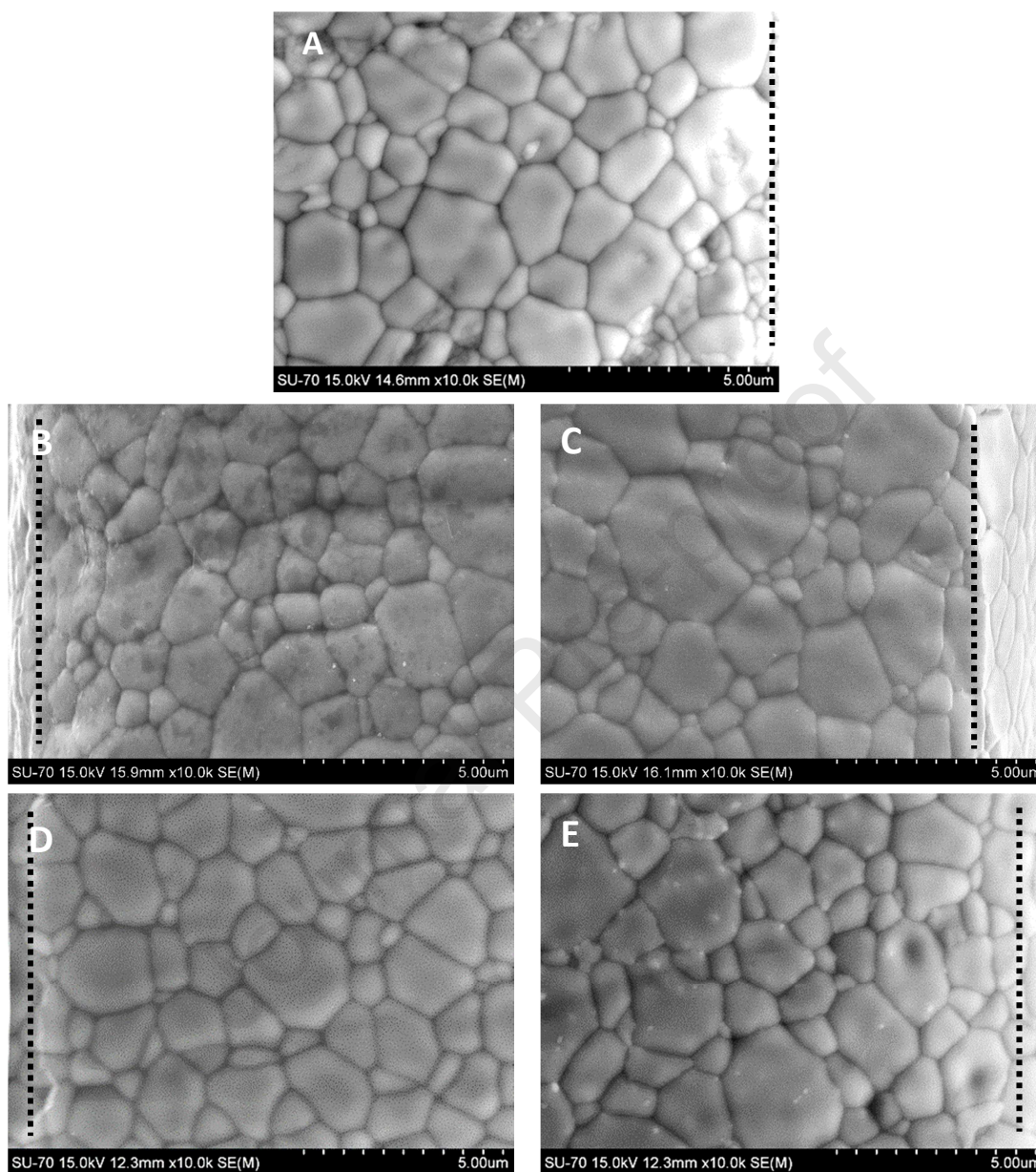

Figure 2. Cross section views of untreated GDC (A), GDC 600 (B, C) and GDC 700 (D, E) samples. The latter images were obtained close to the surface covered by NLC (C, E) or opposite surface, nominally "NLC free" (B, D). The observed surfaces were polished and thermally etched. Dotted lines indicate the approximate disk surface positions.

Table 2. Average grain size of GDC polished and thermally etched after infiltration with NLC at distinct temperatures. Analysis performed close to the NLC covered (top) or "free" sides (bottom), see Figure 1A.

Sample	Average grain size (µm)	
	Top	Bottom
UT	2.44± 0.12	
600	2.99 ± 0.13	2.53 ± 0.11
700	2.75 ± 0.06	2.40 ± 0.07
800 1	3.12 ± 0.09	2.56 ± 0.05
GDCNLC3S*	1.78 ± 0.07	

* Estimated values from SEM images of surfaces without thermal etching.

In order to increase the efficacy of these observations, line scan concentration profiles were also obtained under high magnification (Figure 3). Figure 3A shows the concentration profiles of Ce, Gd and Na across a fracture surface of GDC 800 2. To highlight the grain size, this sample was thermally etched before observation. The fluctuations in concentration are within typical experimental scatter.

Figure 3B shows an equivalent set of information for a fracture surface of GDC 800 1. In this case, thermal etching was avoided to prevent volatilization of any NLC still present in the sample. Since the observation is on polished samples, individual grains cannot be seen. Accordingly, attention was given to specific microstructural features suggesting grain pullouts and/or inter-grain fracture. These consisted of agglomerates of polyhedral voids with dimensions compatible with the previously observed grain size (rounded voids usually correspond to pores). The observed fluctuations in concentration values were mostly within what might be considered experimental uncertainty due to topographical effects and partly overlapping peaks. Even so, a minor deviation from average values might be considered with a central region richer in Na. A faint Na vestige is emphasized here. Clear Na rich spots were absent in all analyses, within the EDS technique resolution.

The analysis of the local chemical composition of all samples is a major challenge in these and similar materials. XRD is only able to provide information on changes in lattice parameters and presence of secondary phases if crystalline and exceeding a reasonable concentration. In this case XRD provided no clear clue on any drift in GDC lattice parameters

8

or presence of secondary phases. The situation with SEM/EDS was just described, only faint evidence was available on the presence of Na in samples after chemical attack with NLC.
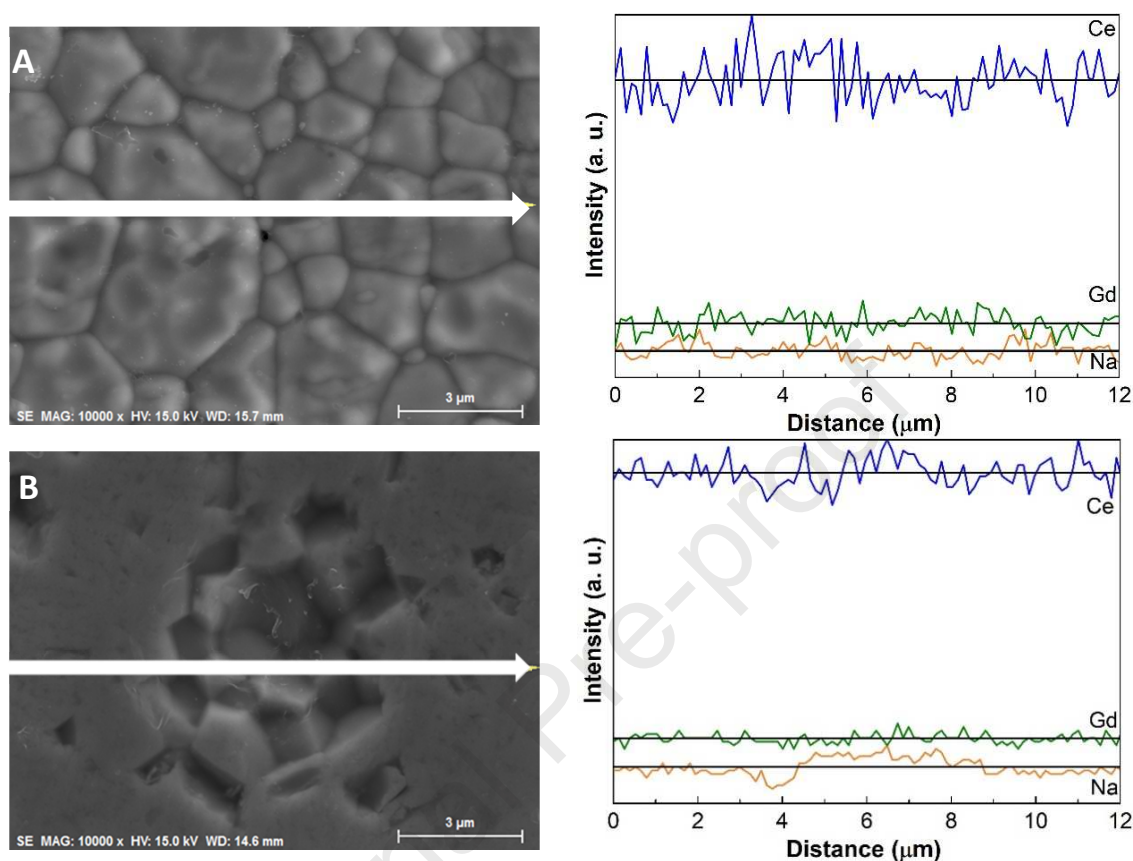

Figure 3. SEM images of polished and thermally etched fracture surfaces of GDC 800 2 (top) or simply polished fracture surface of GDC 800 1 (bottom). Corresponding EDS line scan concentration profiles of Ce, Gd and Na also shown.

Distinct techniques used in the literature (ICP – Inductively Coupled Plasma, SIMS - Secondary-ion mass spectrometry) to inspect similar materials (ceria-based electrolytes with alkali metal salts or oxides used as sintering aids) showed that the overall amounts of alkali metals decreased with increasing firing temperatures (down to vestigial levels with firing temperatures around 1100 °C) due to volatilization [11,13]. TEM (Transmission Electron Microscopy) used in one single study showed the presence of "clean" and "dirty" grain boundaries in GDC pellets fired for 1 hour at 800 °C in a lithium-saturated atmosphere [14]. In any case, multiple materials prepared using distinct routes, showed mostly a degradation of grain boundary conductivity, while others showed conductivity enhancement effects for specific firing conditions and concentrations of sintering aids [11,13]. With a mixed condition ("clean" and "dirty" grain boundaries), their exact role on the global electrical performance is only accessible using sophisticated measurements involving microelectrodes, and a meaningful

9

number of tests is needed to reach any conclusion [21]. An intricated roundabout can be easily created since conditions needed for the observation of a grain boundary surpass those viable for localized electrical measurements.

Alternative techniques like XPS (X-ray Photoelectron Spectroscopy) could be used to detect light elements like Li but the space resolution of this technique is unable to highlight a specific grain boundary composition unless this is converted into an open surface by intergranular fracture. All these comments emphasize that there is no immediate and simple technique to fully disclose the grain boundary characteristics, and information on multiple grain boundaries is mandatory to have a reliable information. On the contrary, evidence on microstructural changes and electrical performance provide reliable sets of information that can be used to build a framework picture on this reality, as attempted in the following sections.

Grain boundaries are the expected favorable pathways for high temperature penetration of molten salts and some of them might even become fully flooded with NLC during thermal treatment. This would explain relatively easy grain pullouts during polishing (or inter-grain facture) as well as some residual alkali metal ions present in these regions (recall Figure 3B). This type of observation and interpretation was already reported in GDC-based materials prepared using sintering aids [14]. No such features were observed in GDC 800 2 since thermal etching promoted the volatilization of residual alkali metal cations present in this sample. In fact, a mild grain growth can be noticed when Figures 3A and 2A are compared (same magnification of 10k). The short thermal treatment (15 min) of GDC during thermal etching at a temperature 10% below the sintering temperature would be unable to explain this effect in the absence of a liquid phase assisted mechanism. As summary, combined SEM/EDS analysis suggests access of residual amounts of NLC to the inside of GDC pellets. Consistently, the NLC treatment at 800 ºC had a higher impact on GDC grain size with respect to treatments at lower temperatures (Table 2).

With the experimental evidence available and background knowledge previously provided on the corrosion of ceramics by molten phases, migration of NLC cations via grain boundaries is the soundest hypothesis to explain small microstructural changes in GDC pellets sintered at 1500 °C and exposed afterwards to NLC at low temperature (800 °C or even below). However, an additional comment is desirable on presumable characteristics of all samples. Within the short time scale of all experiments, impregnation of GDC samples top covered with an NLC layer (Figure 1) corresponds closely to a typical diffusion problem where the source of diffusing species has a constant concentration (NLC layer). As such, the concentration of any diffusing species across the pellets should depend on time and distance to the top surface. The typical solution of the Fick's second law for planar diffusion and a given set of boundary conditions includes the well-known error function and time dependent concentration profiles

[22]. Due to the analytical limitations previously discussed there was no chance to quantify the presence of alkali metal cations across the cell thickness. However, these considerations are fully consistent with distinct characteristics of GDC pellets from top to bottom, as evidenced during the previous discussion on grain sizes (recall Table 2 and inherent data examination). Lastly, this means that distinct treated GDC "layers" should offer distinct parallel electrical pathways from top to bottom, when the so-called in-plane electrode arrangement is adopted (Figure 1), since the applied electric field is perpendicular to the dominant diffusion direction.

The entire discussion up to now addressed only GDC materials exposed to NLC after sintering. In GDCNLC3S sintered at 1100 °C for 4 h, all cations were intimately mixed already as precursors. Figure S3 (Supplementary Information) shows a regular microstructure of GDCNLC3S, with grain size only slightly smaller than observed for GDC 800 2 (Table 2). The densification level was high (>95%), as observed for GDC sintered at 1500 °C for 4 h also. The close microstructural characteristics of GDCNLC3S sintered at 1100 °C with respect to pure GDC highlights the efficacy of the processing route (reactive powders) complemented by the NLC sintering aid effect. Also, as noticed for GDC 800 2 (Figure S2), atomic number maps of GDCNLC3S (Figure S3) showed no preferential location of Na in the bulk or along grain boundaries. Within the resolution of EDS, all samples were mostly chemically homogeneous.

3.2 Impedance spectroscopy

Analysis of impedance spectroscopy data is the usual source of previously claimed bulk and grain boundary conductivity enhancements. Special attention to published results suggests lacking details providing proper validation of impedance spectra deconvolution (e.g., overlapping electrode and grain boundary arcs), consistent identification of impedance arcs (e.g., proper attention to relaxation frequencies) and other possible sources of error. This assumption justifies the attention dedicated in the following paragraphs to specific solutions adopted in this work, aiming at proper validation of presented data.

3.2.1 Setup and cell characteristics

Normal handling of impedance spectroscopy data includes normalization of raw data against cell dimensions. Distinct cell geometries impact the magnitude and ability to properly deconvolute impedance spectra. Also, normal setup stray capacitances can influence the analysis of high frequency impedance data but are marginal when grain boundary performance is considered. Due to their relevance in this work, these aspects will be firstly addressed before analysis of actual data.

Typical sets of impedance spectroscopy data at low temperature usually show three distinct arcs, the so-called bulk, grain boundary and electrode contributions (Figure 4) [23]. The simplest equivalent circuit able to describe this situation includes a series arrangement of three parallel $R_i \| C_i$ elementary circuit elements, where i stands for bulk (b), grain boundary (gb) or electrode (el) contributions (Figure 4 inset). R_i is a resistor and C_i a capacitor. Deviation from ideal pure capacitor behavior is taken into consideration with the replacement of C elements by constant phase elements (CPE). In the comments below only the simplest case (pure C elements) will be considered.
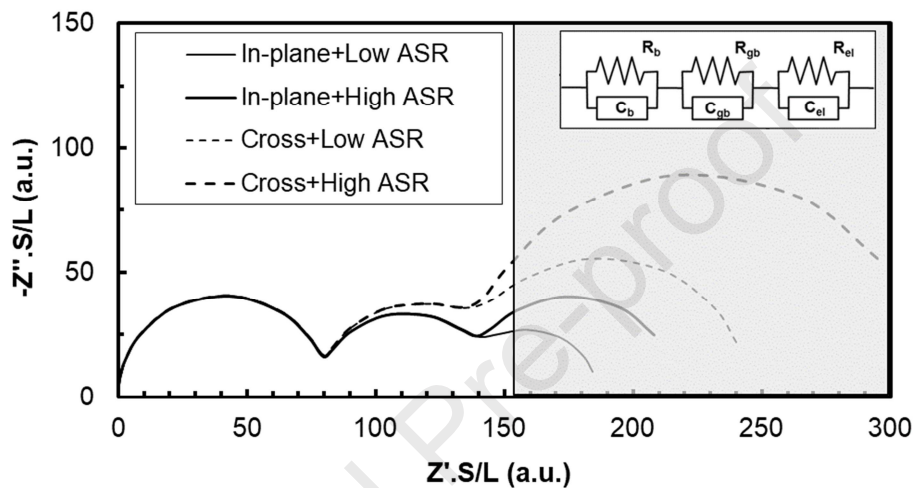

Figure 4. Estimated effect of distinct cell geometries and electrode configurations on impedance spectra characteristics (see text for details). The assumed equivalent circuit is shown as an inset. The shaded area is often outside the available frequency range at low temperature (e.g., see Figure 5).

For fully dense polycrystalline ceramic electrolytes with similar microstructures, under specific working conditions (e.g., temperature and oxygen activity) the bulk and grain boundary R depend only on cell dimensions (S and L) and their intrinsic conductivities. On the contrary, the electrode resistance depends only on the electrode surface area (S) and corresponding area specific resistance (ASR). As such, normalization of impedance data (real and imaginary parts, Z' and Z", respectively) is often based on the cell geometric factor (S/L) when assessing bulk and grain boundary transport properties, or based on the electrode area (S), when measuring mostly electrode performance.

As shown in Figure 1B, the in-plane electrode geometry adopted as relevant cell dimensions the cell length (distance between electrodes, L) and cell rectangular cross section (S=a.b, with a and b the circle segment chord and disk thickness, respectively). For electrodes deposited on the upper and lower pellet surfaces (cross measurements), the corresponding parameters are the pellet thickness (L) and electrode surface area (S=$\pi.r^2$, with r being the radius

12

of the electrode area). This easily yields distinct S/L geometric factors. In the present experiments, S/L values covered more than one order of magnitude (0.27 to 4.9 cm).

Figure 4 shows four impedance spectra inspired on actual data presented later (Figure 5), where two distinct (high and low) ASR values and two different sets of cell dimensions (in-plane and cross electrode arrangements) are combined. Bulk and grain boundary conductivity were preserved in all calculations. Normalization of simulated impedance data against cell dimensions (S/L) should yield similar results except for the electrode arc. However, while the high frequency arc (bulk) is mostly insensitive to distinct situations, the grain boundary arc can be easily disturbed for large electrode impedances (large ASR). The situation is aggravated when relaxation frequencies of grain boundary and electrode processes are close.

Figure 4 highlights that deconvolution between grain boundary and electrode arcs becomes much simpler using the in-plane electrode geometry (small S/L). The rationale is obvious. The absolute magnitudes of bulk and grain boundary resistances increase with cell length while the electrode impedance is only sensitive to the electrode surface area. When raw impedance data is normalized with respect to the geometric factor (S/L) the "relative" electrode impedance decreases with increasing cell length.

Figures 5A and 5B show the corrected impedance spectra of untreated or NLC infiltrated GDC for several temperature/dwell time combinations, obtained using both electrode configurations, in air, at 200 ºC. These spectra show two arcs corresponding to the usual bulk (high) and grain boundary (low) frequency ranges. An equivalent circuit containing two elementary parallel R‖CPE circuits arranged in series could be easily used to fit impedance plots below 350 ºC. Part of the electrode arc (low frequency) is visible in the cross configuration but hardly discernible in the in-plane configuration. The reasons for this difference were previously discussed.

For pure GDC tested in the cross and in-plane electrode configurations, the bulk arcs should be fully superimposed, according to the previous discussion. On the contrary, the grain boundary arc might suffer from distinct electrode arc overlapping. In fact, the bulk conductivity values obtained with the experimental geometric factors of these cells showed a slight difference, temperature dependent. Using bulk conductivity as reliable reference, the geometric factor relation (cells Cross versus UT) at 200 °C should be 18.3 and was 15.8. Matching of both values increased with increasing temperature (18.3 versus 18.0 at 500 °C), indicating a slight drift with temperature in the relative positions of equipotential lines in the in-plane configuration. To minimize the impact of this parameter on other estimates, the GDC bulk conductivity obtained with the cross configuration was used as reference. This allowed an easy correction of the in-plane geometric factor, when required (lower temperatures only). This small

13

correction had no impact on all trends discussed in the following sections, but is of great importance to facilitate the direct visual analysis of data in Figure 5, where these corrections are adopted.
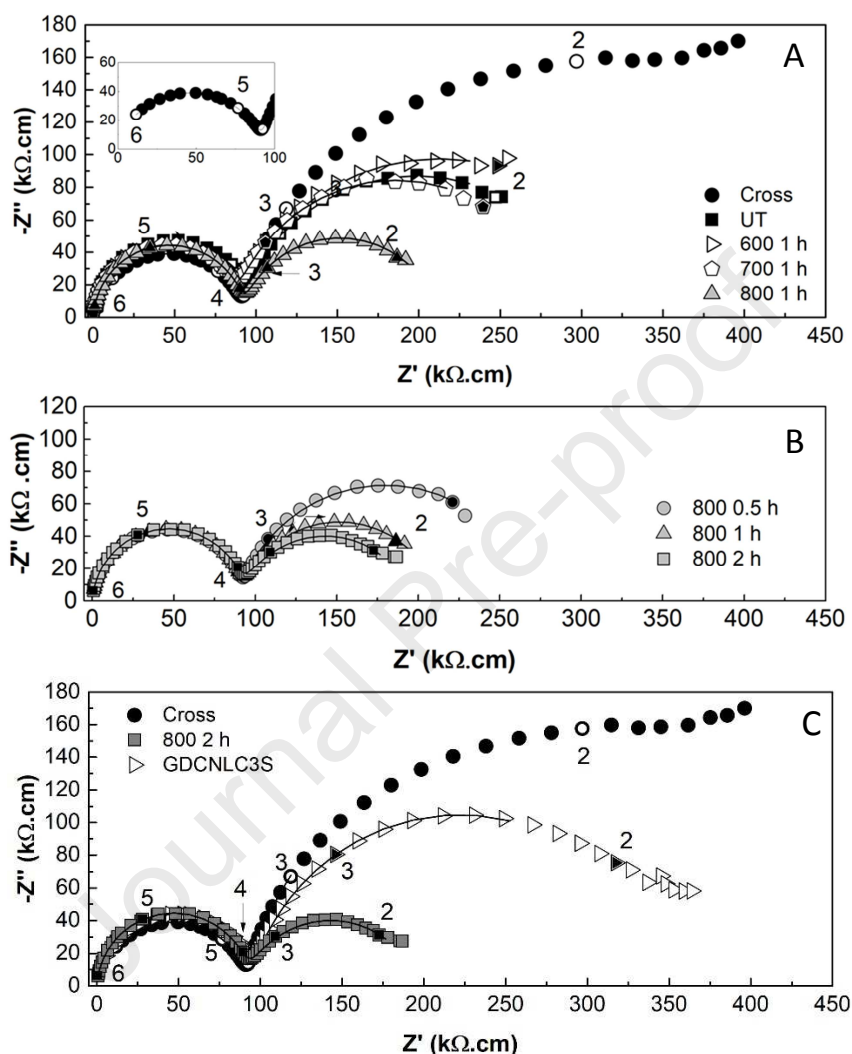

Figure 5. Impedance spectra in air, at 200 ºC, of GDC-based cells with surfaces untreated or treated with NLC at 600-800 ºC for 1 h (A), or at 800 ºC for different times (B). A GDCNLC3S cell is also considered for comparison (C). The inset in (A) details the Cross cell high frequency data distribution. Numbers correspond to the log of frequency (Hz).

Another relevant experimental feature involved in distinct cell configurations is an obvious mismatch between the apparent relaxation frequencies of the bulk arcs of Cross and all in-plane cells. These should be independent of the cell geometry, but they appear as dependent, almost one order of magnitude different (Table 3). This can be easily perceived from inspection of Figure 5A. The bulk arcs extend almost to the axes origin for the in-plane electrode

14

arrangement. For the cross-cell measurement (Figure 5A inset), the arc ends well before the axes origin. This result is a consequence of the cell stray capacitance (C_s), feature often ignored in the analysis of impedance data.

Table 3. Estimated bulk and grain boundary electrical parameters (from impedance spectra), including the stray capacitance (C_s) correction (see text for meaning of symbols).

Cell	T (°C)	Bulk				Grain boundary	
		Estimates (raw data)		After correction for C_s		Estimates (raw data)	
		C_t (pF)	ω_r (rad.s^{-1})	C_{cell} (pF)	$\omega_{r,bulk}$ (rad.s^{-1})	C_{est} (nF)	ω_r (rad.s^{-1})
Cross	200	30.6	1.76×10^6	23.8	2.27×10^6	12.8	1.03×10^3
	250	28.9	1.11×10^7	21.9	1.47×10^7	13.5	8.03×10^3
UT	200	9.96	2.26×10^5	3.12	7.22×10^5	0.688	1.39×10^3
	250	9.82	1.38×10^6	2.83	4.81×10^6	0.682	2.84×10^4

C_s is due to the utilization of small diameter parallel electrical (Au) wires separated by thin alumina walls, as electrical connections to the outside equipment. Accordingly, C_s and the bulk cell capacitance (C_{cell}) are arranged in parallel and should add to each other:

$$C_t = C_s + C_{cell} \tag{1}$$

C_t, the total capacitance, can be estimated from raw high frequency impedance data ("bulk" arc), after proper conversion of the CPE element magnitude into true capacitance. Also, the real bulk cell capacitance can be obtained from the relative dielectric constant of GDC (ε_r) and cell dimensions:

$$C_{cell} = \varepsilon_o \, \varepsilon_r \, S/L \tag{2}$$

with ε_o being the vacuum dielectric constant (8.85×10^{-12} F/m).

With the availability of several cells with distinct S/L ratios, combination of equation (2) with equation (1) can be used to estimate C_s and ε_r. The exercise is shown in Figure S4 (see Supplementary Information), including two sets of results obtained with multiple cells at two distinct temperatures (200 and 250 °C). The slope of each trend line is the bulk dielectric constant of GDC while the intercept is C_s. As expected for the phenomena involved, values obtained at slightly distinct temperatures yield similar results, 6.84 and 6.99 pF for C_s, and 55 and 51 for ε_r, at 200 and 250 °C, respectively. ε_r is slightly higher than values often reported [24] and C_s is slightly lower than estimates for similar setups [25]. However, alternative estimates of C_s based on simplified analytic solutions derived for coplanar electrodes in sensors

15

yield similar orders of magnitude [26]. Irrespective of some uncertainty, the obtained C_s value can be used to correct bulk capacitance and relaxation frequency estimates from raw impedance data, as shown in Table 3. The consequence is a much closer matching between relaxation frequencies of samples with distinct geometry. The much lower bulk capacitance of in-plane cells is a normal consequence of the cell geometry, with larger spacing between electrodes of smaller area. As mentioned, if C_s is slightly underestimated, a higher value would improve the agreement in relaxation frequencies since C_s is the C_t dominant contribution in the UT cell, at high frequency.

The previous discussion emphasized the mismatch in the bulk arc relaxation frequency. Unlike for the bulk arc, the impact of C_s on the grain boundary arc is almost negligible, since the magnitude of capacitance values involved is different (almost three orders of magnitude higher for the grain boundary, see Table 3). This means that the grain boundary arc relaxation frequencies obtained from raw impedance data can be securely used to compare the electrical characteristics of distinct materials, as exploited in the following section.

3.2.2 Electrochemical performance of GDC-based electrolytes

Figure 5A shows the electrical performance of GDC-based cells without or with infiltrated NLC, at distinct temperatures. A significant reduction of the magnitude of the grain boundary arc is observed when the NLC infiltration temperature increases from 600 to 800 °C. In reality, the major change occurs between 700 and 800 °C, resulting in a grain boundary arc even smaller than observed for the cell without thermal treatment (UT), with the same electrode configuration.

Figure 5B shows the impact of distinct durations (0.5, 1 and 2 h) of NLC infiltration at 800 °C on the electrical properties of GDC. The improvement in grain boundary conductivity with the duration of the treatment is in many aspects similar to the previous role of temperature on electrical performance. The roles of time and temperature suggest thermally activated diffusion/reaction processes involved in the observed changes. These effects are quite reproducible as shown with distinct samples and ac signal magnitudes (0.5 or 1 V), situation presented in Figure 6.
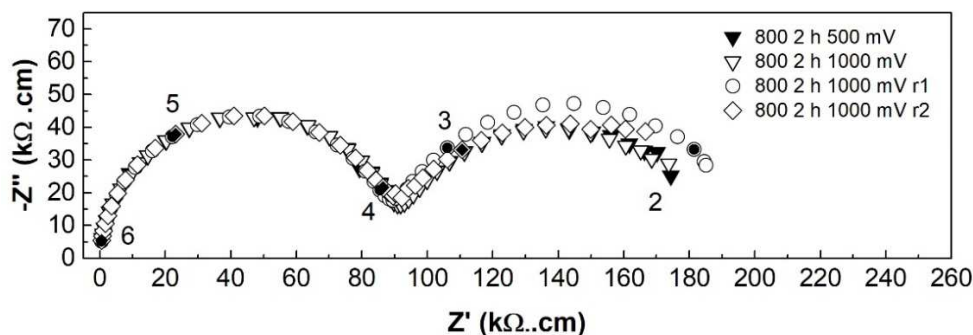
16

Figure 6. Impedance spectra in air, at 200 ºC, of several GDC-based cells infiltrated with NLC at 800 ºC for 2 h. Replicas are depicted as r1 and r2. Numbers correspond to the log of frequency (Hz). Also shown data obtained with distinct a.c. signals.

All sets of data considered up to this point involved dense GDC cells as starting point. To assess the possible direct impact of NLC on GDC, impedance spectroscopy measurements were also performed with GDCNLC3S. The corresponding results are shown in Figure 5C. The performance of GDC 800 2 is better than observed for GDCNLC3S where all cations were intimately mixed. Furthermore, both sets of materials showed better performance than standard pure GDC.

Figure 7A shows typical Arrhenius-type plots of total conductivity (σ_t) of all samples within the exploited temperature range (200-600 ºC). The conversion of resistance into conductivity ($\sigma=L/S.R$) assumed the cell dimensions previously discussed. The option for plots of $\ln(\sigma_t.T)$ versus $1/T$ means that the slopes of all lines can be used to estimate ion migration energies (E_m, Table 4) instead of simple activation energies. A slight spread in σ_t values at low temperature vanishes with increasing temperature. At 600 ºC, conductivity values of 1.9×10^{-2} and 1.8×10^{-2} Scm^{-1} were obtained with pure GDC for in-plane and cross measurements, respectively, but the best conductivities were observed for GDC 800 1 and GDC 800 2, with values reaching up to 2.2×10^{-2} Scm^{-1}. Overall, the migration energies, within the entire 200 to 600 ºC temperature range, were in the narrow 76.6 - 80.9 kJ.mol^{-1} span (Table 4).

Figure 7B shows similar Arrhenius-type plots for bulk conductivity (σ_b) within the lower temperature range, where reliable data deconvolution could be performed. An almost overlapping line of GDCNLC3S with respect to the remaining GDC-based samples is obvious. All samples have close σ_b values with migration energies varying in the narrow 73.0 - 74.1 kJ.mol^{-1} range, indicating a similar dominant ionic transport mechanism in all materials.

Figure 7C shows Arrhenius-type plots for grain boundary conductivity (σ_{gb}). The same scales were adopted in Figures 7B and 7C to show that σ_{gb} values are rather distinct, as already noticed in the analysis of impedance spectra (see also Table 4). The advantage of GDC 800 1 and GDC 800 2 with respect to pure GDC and even GDCNLC3S is clear.

17

Relaxation frequencies of impedance spectroscopy arcs can be used as fingerprints of relevant polarization phenomena. This aspect is in the core of impedance spectroscopy efficacy in the separation of distinct contributions. As such, the analysis of the relaxation frequency of grain boundary arcs is also considered in a typical Arrhenius-type plot (Figure 7D) within the 200-300 ℃ temperature range. The spread in actual values is small but the grain boundary relaxation frequency increases with duration of NLC treatment (at 800 ℃), reaching values close to those observed for GDCNLC3S.
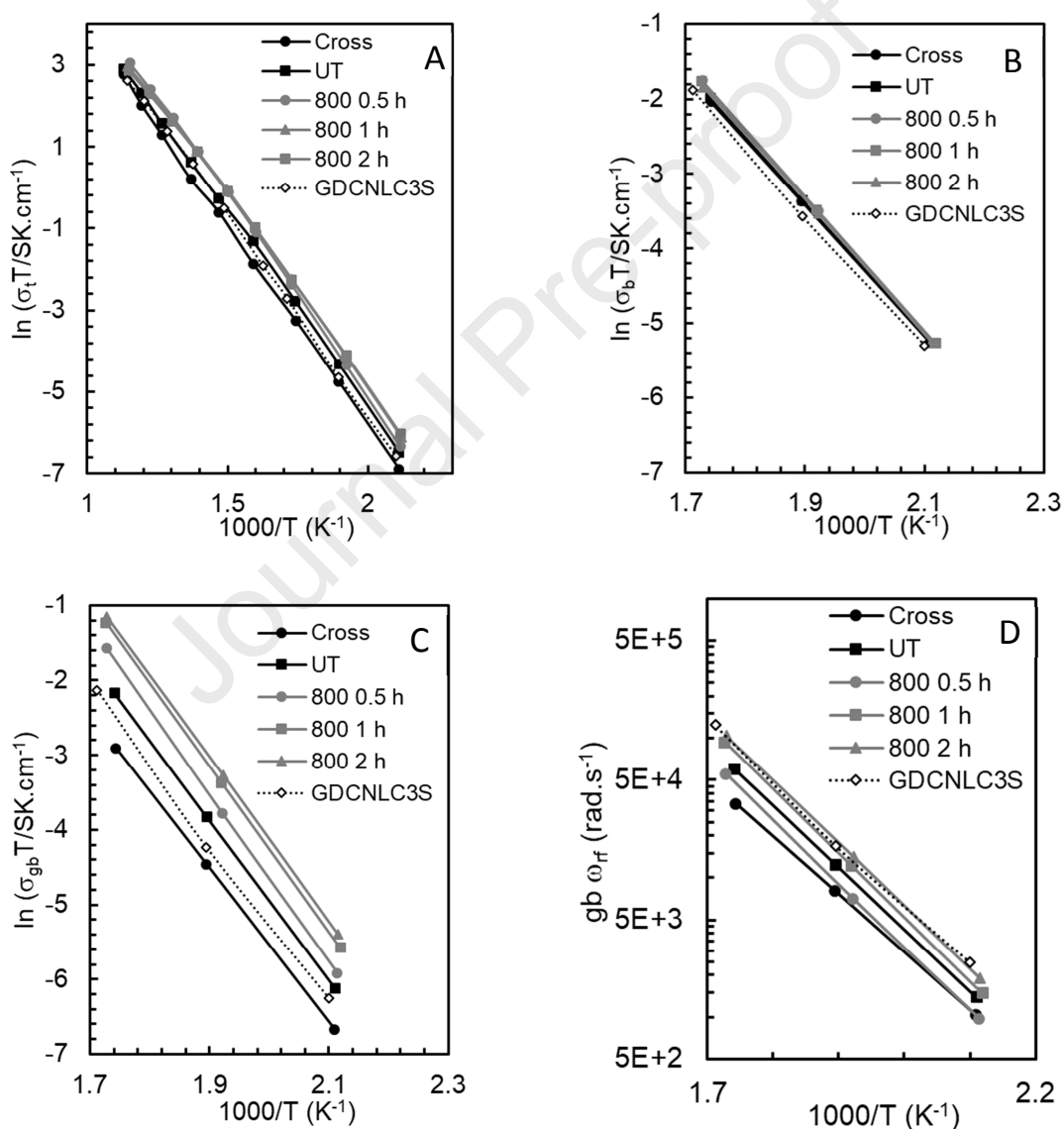

Figure 7. Arrhenius-type plots of the total conductivity (A), bulk conductivity (B), grain boundary conductivity (C), and grain boundary relaxation frequency (D) of several GDC-based samples.

Table 4. Electrical conductivity (σ, S.cm^{-1}) and migration energy (E_m, kJ.mol^{-1}) of tested GDC-based electrolytes

Sample	Total		Bulk		Grain boundary	
	σ_t ($\times 10^{-2}$) 600 °C	E_m (200-600 °C)	σ_{bulk} ($\times 10^{-4}$) 300 °C	E_m (200-600 °C)	σ_{gb} ($\times 10^{-4}$) 300 °C	E_m (200-300 °C)
Cross	1.79	80.9	2.28	73.2	0.95	85.3
UT	1.87	78.7	2.38	73.7	2.00	88.9
800 0.5	1.83	78.0	2.35	73.4	3.00	93.0
800 1	2.20	77.6	2.53	74.1	5.04	91.9
800 2	2.00	76.6	2.41	73.7	5.43	91.1
GDCNLC3S	1.55	80.5	1.94	73.0	1.40	88.2

Irrespective of the mentioned differences, combined analysis of all data sets shows no evidence for a change in dominant charge carrier with NLC infiltration. Migration energies (bulk and grain boundary) for all samples remained within typical values for GDC. The sharp total conductivity changes often observed in GDC+NLC composites around the NLC eutectic temperature (1000/T≈1.3 K^{-1}), are absent in these results [27,28]. These aspects are stressed here to emphasize that alkali metal ions and/or associated anions (e.g., CO_3^{2-}) seem irrelevant in these materials as charge carriers.

3.3 Final comments

The bulk electrical performance of pure GDC and NLC infiltrated samples matched closely the electrical performance of GDCNLC3S. In the latter case all cations were intimately mixed as precursors. Substantial dissolution of alkali metal cations in the ceria lattice seems hardly sustainable. Even Li$^+$, the closest in size with respect to Ce^{4+} (radii for VIII coordination: 97 (Ce^{4+}), 92 (Li$^+$) and 118 pm (Na$^+$) [29]) should originate enhanced concentrations of oxygen vacancies and strong defect interaction (triple negative acceptor dopant and the double positive oxygen vacancies, Li$_{Ce}'''$ and $V_O^{\bullet\bullet}$ using the Kroger-Vink notation). This should be visible either in the magnitude of bulk conductivity or in ionic migration energy. There was no serious evidence for any of these effects.

The electrical performance of grain boundaries of polycrystalline acceptor-doped oxide-ion conductors is determined by the local distribution of dopant cations and oxygen vacancies. In GDC and similar materials, the electrical grain boundary includes space-charge layers near the positively charged grain boundary core. Depletion of oxygen vacancies in the space-charge layers and accumulation of acceptor dopants near the grain boundary core are interrelated [30,31]. This explains the poor grain boundary conductivity observed even in high purity materials.

19

Depletion of Gd cations from the outer GDC grain layers due to chemical interaction with the alkali carbonates (selective lixiviation) and/or formation of new local chemical environments might lead to a charge and defect redistribution, including leveling of concentration of oxygen vacancies in the grain boundary region with respect to the bulk. This reasoning was used to explain the role on grain boundary conductivity of an added second phase involving the formation of a liquid. In this situation, the grain boundary conductivity increased with respect to the original condition [32].

The electrical properties of grain boundaries can also drastically change due to impurity effects. Oxides like SiO_2 might accumulate in the grain boundaries during sintering, creating a blocking effect with respect to ionic conduction [33]. On the contrary, grain boundary scavenging effects, corresponding to the removal of secondary phases to triple contact points by combination with a scavenger agent, would be consistent with an enhanced grain boundary conductivity [34,35]. Specific scavengers instead of (besides) removing a secondary phase from the grain boundary might also change the local concentration of species like the acceptor dopant.

Previously suggested mechanisms are within what might be identified as state of the art knowledge on grain boundary tuning effects. Recently, alternative grain boundary conductivity enhancement mechanisms considered local collaborative transport of molecular and ionic species involving alkali metals and oxygen [12]. To examine this possibility a series of additional experiments was performed, polarizing the NLC treated cells with a dc current. Under dc polarization, reduction of oxygen to oxide ion and oxidation of oxide ions to oxygen (cell cathodic and anodic reactions) should proceed without disturbance since open air is a source and sink for oxygen. However, reactions involving alkali metal ions cannot be sustained due to the absence of proper sources/sinks for these species at the electrode/electrolyte surface in air. Accordingly, mechanisms involving mobile alkali ions should vanish with dc polarization. The dc polarization experiment was performed for almost 400 min at 500 °C, in air. The applied dc voltage was 0.5 V, and the dc current was around 0.15 mA, showing a slight steady increase after a short initial induction period (Figure 8A).

The impedance spectra of GDC 800 2 cells at 200 °C before and after polarization are shown in Figure 8B. Both sets of data almost overlap. There is no sign of degradation of bulk or grain boundary conductivity. Under dc conditions, in the presence of a percolated pathway for mobile alkali ions, these should be dragged to the cell cathode side. If mobile and present in isolated pools along grain boundaries, these should accumulate in one side while their counter negative ions should accumulate in the opposite side. The absence of any visible changes in the grain boundary arc suggests that the local characteristics were preserved. This experiment

20

shows that direct participation of mobile alkali metal ions in the grain boundary transport mechanism is not easily defendable.

In order to understand the reason for the slight current enhancement with time (Figure 8A), impedance spectra were also recorded at 500 °C, before and after polarization (Figure 8C). The electrode arc showed a visible reduction in magnitude. SEM inspection showed that the anode microstructure was improved under polarization (increasing porosity). An improved electrode microstructure (enhanced triple phase boundary line) facilitated oxygen release in the anode side and decreased the electrode impedance, with a positive impact on the total cell impedance.
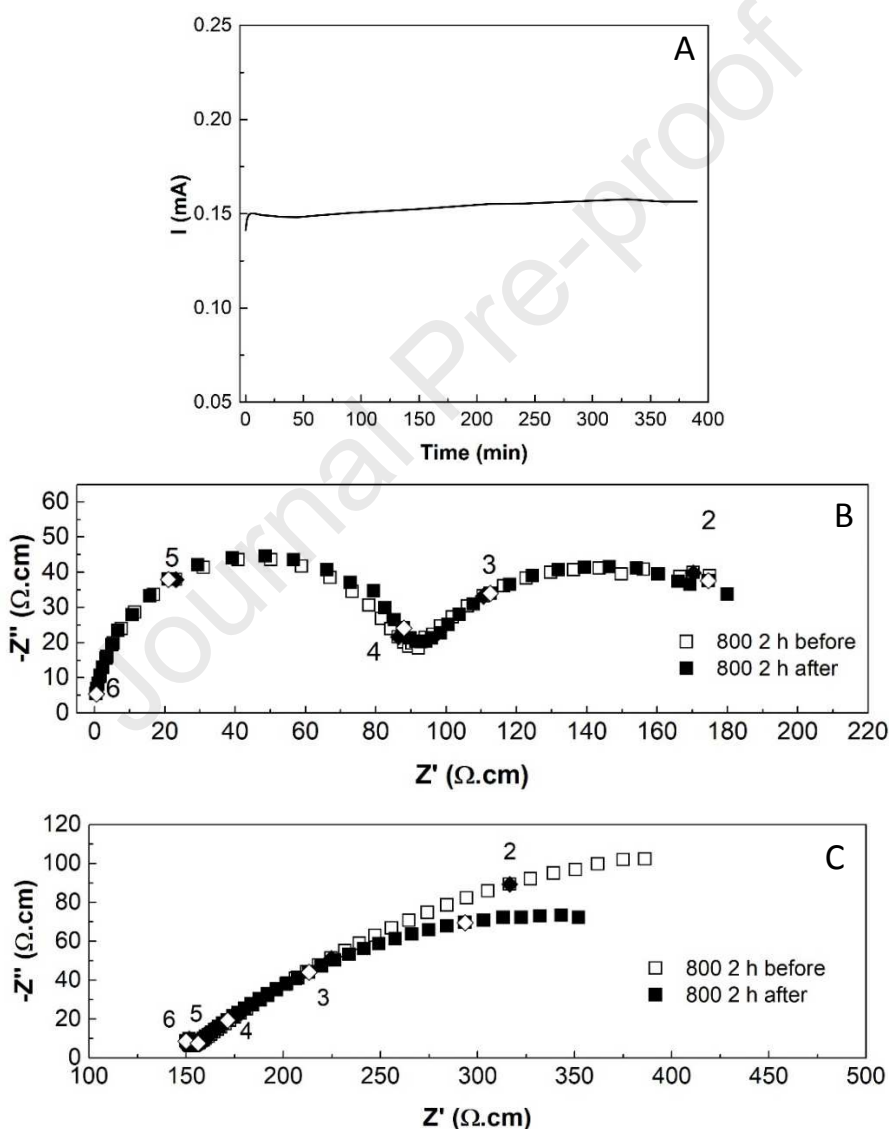

Figure 8. (A) Time dependence of the imposed current, at constant dc voltage of (0.5 V), across a GDC 800 2 cell. Impedance spectroscopy data obtained at 200 °C (B) and 500 °C (C) before (open symbols) and after (filled symbols) cell polarization. Numbers correspond to the log of frequency (Hz).

There is probably no single mechanism able to explain the entire set of effects observed in materials where alkali metal salts are introduced in minor amounts. One first issue deserving consideration is the distinct tendency of Ce and Gd oxides to react with alkali metal carbonates in air [36]. The first oxide is reasonably stable up to 1000 °C, the second oxide tends to react already at 900 °C with formation of a mixed Li and Gd oxide:

$$Gd_2O_3 + Li_2CO_3 \rightarrow 2\ LiGdO_2 + CO_2 \tag{3}$$

The distinct tendency for reaction in air is even more relevant when in the presence of CO_2 (likely, due to the partial thermal decomposition of alkali metal carbonates). In this case, CeO_2 is stable up to 1000 °C but Gd_2O_3 starts reacting at temperatures as low as 500 °C, forming a dioxycarbonate ($Gd_2O_2CO_3$) [37]. This means that alkali metal carbonates might act as selective Gd scavengers from grain boundaries at moderate temperatures.

Understanding the reported electrical conductivity data also needs a framework understanding of the likely infiltration mechanism. During early impregnation stages (low temperature and low duration) only outside grains are partly covered by NLC. Since the carbonate phase at low temperature is an insulator (lower conductivity than GDC [38]), these regions of the material become ion-blocking. The presence of a dispersed insulator within an oxide ion-conductor might appear predominantly in the so-called grain boundary arc or in both bulk and grain boundary arcs, always as impedance enhancement. This would qualitatively explain the trends observed with the GDC 600 cell. This material performed worse than pure GDC in all aspects.

The bulk conductivity of samples 800 1 and 800 2 is the same as pure GDC but the grain boundary arc conductivity is much higher. A mechanism to explain the disappearance of the suggested blocking phase is needed. The temperature of 800 °C exceeds the eutectic temperature (500 °C), volatilization and decomposition of NLC (to oxides) should be noticeable. Chemical interaction with Gd along the grain boundaries is also expected, as previously detailed. At 800 °C both NLC and outer GDC grain regions are in direct contact with each other and are changing. Prolonged treatments at 800 °C favor previously suggested Gd scavenging effects, with potential positive consequences on the grain boundary electrical performance. Formation of isolated particles of secondary phases could not be detected by SEM/EDS. These might include mixed Gd and alkali metal oxides concentrated in triple contact points. Besides this, dragging of Gd from the grain boundary to outside the GDC pellet is feasible in the presence of a molten phase. Extraction of corrosion products via a liquid phase is well known from pitting corrosion via grain boundaries in metals.

These final remarks highlight several possible mechanisms that might contribute to the observed grain boundary conductivity enhancement. Full demonstration of any of these mechanisms involves lengthy and demanding experiments (e.g., analysis of concentration profiles in multiple grain boundaries, measurement of specific grain boundary conductivities). In fact, in similar ceramic materials grain boundaries show a distribution of conditions, from clean to wet by a secondary phase [12], justifying a wide screening of situations. Irrespective of the exact mechanism(s) involved, the effect is obvious and can be used to improve the grain boundary of standard dense solid electrolytes like GDC. The capability to fully reproduce the conductivity enhancement obtained with NLC impregnation using a simpler procedure is an obvious pending challenge.

4. Conclusions

GDC pellets heat treated with NLC showed improved grain boundary conductivity. These materials showed better performance than standard GDC or even competitive GDC+NLC ceramic electrolytes prepared by a chemical route. Microstructural changes induced by the penetration of NLC via grain boundaries were found marginal within the resolution of standard SEM/EDS capabilities. Chemical changes in the outer layers of GDC grains seem a plausible explanation for the conductivity enhancement. The existence of local or percolating contributions/pathways involving extrinsic (NLC derived) ions was ruled out after dc polarization measurements showing no impact on the material conductivity. Overall, the present results introduce a promising perspective in the field of grain boundary tuning of dense ceramics.

5. References

[1]   H. Inaba, H. Tagawa, Ceria-based solid electrolytes, Solid State Ionics. 83 (1996) 1–16.

[2]   V. V. Kharton, F.M. Figueiredo, L. Navarro, E.N. Naumovich, A. V. Kovalevsky, A.A. Yaremchenko, A.P. Viskup, A. Carneiro, F.M.B. Marques, J.R. Frade, Ceria-based materials for solid oxide fuel cells, J. Mater. Sci. 36 (2001) 1105–1117.

[3]   J. Van herle, T. Horita, T. Kawada, N. Sakai, H. Yokokawa, M. Dokiya, Low temperature fabrication of (Y,Gd,Sm)-doped ceria electrolyte, Solid State Ionics. 86–88 (1996) 1255–1258.

[4]   V. V Kharton, F.M.B. Marques, A. Atkinson, Transport properties of solid oxide electrolyte ceramics: a brief review, Solid State Ionics. 174 (2004) 135–149.

[5]   H.J. Avila-Paredes, S. Kim, The effect of segregated transition metal ions on the grain boundary resistivity of gadolinium doped ceria: Alteration of the space charge potential, Solid State Ionics. 177 (2006) 3075–3080.

[6]   E.Y. Pikalova, A.N. Demina, A. k. Demin, A.A. Murashkina, V.E. Sopernikov, N.O. Esina, Effect of Doping with Co_2O_3, TiO_2, Fe_2O_3 , and M_2O_3 on the Properties of $Ce_{0.8}Gd_{0.2}O_{2-\delta}$, Inorg. Mater. 43 (2007) 830–837.

[7]   K. Neuhaus, S. Baumann, R. Dolle, H.-D. Wiemhöfer, Effect of MnO_2 Concentration on the Conductivity of $Ce_{0.9}Gd_{0.1}Mn_xO_{2-\delta}$, Crystals. 8 (2018) 40.

[8]   T.S. Zhang, L.B. Kong, Z.Q. Zeng, H.T. Huang, P. Hing, Z.T. Xia, J. Kilner, Sintering behavior and ionic conductivity of $Ce_{0.8}Gd_{0.2}O_{1.9}$ with a small amount of MnO_2 doping, J. Solid State Electrochem. 7 (2003) 348–354.

[9]   J.D. Nicholas, L.C. De Jonghe, Prediction and evaluation of sintering aids for Cerium Gadolinium Oxide, Solid State Ionics. 178 (2007) 1187–1194.

[10]   S. Li, C. Xian, K. Yang, C. Sun, Z. Wang, L. Chen, Feasibility and mechanism of lithium oxide as sintering aid for $Ce_{0.8}Sm_{0.2}O_\delta$ electrolyte, J. Power Sources. 205 (2012) 57–62.

[11]   T. Zhu, Y. Lin, Z. Yang, D. Su, S. Ma, M. Han, F. Chen, Evaluation of Li_2O as an efficient sintering aid for gadolinia-doped ceria electrolyte for solid oxide fuel cells, J. Power Sources. 261 (2014) 255–263.

[12] A. Maheshwari, H. Wiemhöfer, Augmentation of grain boundary conductivity in Ca^{2+} doped ceria-carbonate-composite, Acta Mater. 103 (2016) 361–369.

[13] M. Han, Z. Liu, S. Zhou, L. Yu, Influence of Lithium Oxide Addition on the Sintering Behavior and Electrical Conductivity of Gadolinia Doped Ceria, J. Mater. Sci. Technol. 27 (2011) 460–464.

[14] Jason Dale Nicholas, Low Temperature Constrained Sintering of Cerium Gadolinium Oxide Films for Solid Oxide Fuel Cell Applications, PhD Thesis, University of California, 2007.

[15] J.P.F. Grilo, D.A. Macedo, R.M. Nascimento, F.M.B. Marques, Electronic conductivity in Gd-doped ceria with salt additions, Electrochim. Acta. 318 (2019) 977–988.

[16] J.P.F. Grilo, D.A. Macedo, R.M. Nascimento, F.M.B. Marques, Performance of GDC with alkali metal carbonates as sintering aids, Solid State Ionics. 346 (2020) 115221.

[17] E. Gomes, F.M. Figueiredo, F.M.B. Marques, Mixed conduction induced by grain boundary engineering, J. Eur. Ceram. Soc. 26 (2006) 2991–2997.

[18] O. Schulz, M. Martin, Preparation and characterization of $La_{1-x}Sr_xGa_{1-y}Mg_yO_{3-(x+y)/2}$ for the investigation of cation diffusion processes, Solid State Ionics. 135 (2000) 549–555.

[19] N.S. Jacobson, K.N. Lee, Corrosion of mullite by molten salts, J. Am. Ceram. Soc. 79 (1996) 2161–2167.

[20] B. Cela, D.A. de Macedo, G.L. de Souza, A.E. Martinelli, R.M. do Nascimento, C.A. Paskocimas, NiO–CGO in situ nanocomposite attainment: One step synthesis, J. Power Sources. 196 (2011) 2539–2544.

[21] J. He, J. Liu, J. Hu, R. Zeng, W. Long, Non-uniform ageing behavior of individual grain boundaries in ZnO varistor ceramics, J. Eur. Ceram. Soc. 31 (2011) 1451–1456.

[22] J. Crank, The Mathematics of Diffusion, Clarendon Press Oxford. 2 (1975).

[23] J. Maier, On the Conductivity of Polycrystalline Materials, Berichte Der Bunsengesellschaft Für Phys. Chemie. 90 (1986) 26–33.

[24] N.H. Perry, T.C. Yeh, T.O. Mason, Temperature dependence of effective grain core/single crystal dielectric constants for acceptor-doped oxygen ion conductors, J. Am. Ceram. Soc. 94 (2011) 508–515.

[25] A.I.B. Rondão, S.G. Patrício, F.M.L. Figueiredo, F.M.B. Marques, Impact of ceramic matrix functionality on composite electrolytes performance, Electrochim. Acta. 109 (2013) 701–709.

[26] V. Armijo, L. Atencio, M.L. Brooks, D.M. Lee, J.B. McClelland, C.L. Morris, P.L. McGaughey, M. Rawool-Sullivan, W.E. Sondheim, Cathode Strip Readout Chamber Design Issues, in: LANL Rep. R&D Progr. Cathode Strip Readout Chambers PHENIX Muon Track. Syst., n.d.

[27] M. Benamira, A. Ringuedé, L. Hildebrandt, C. Lagergren, R.N. Vannier, M. Cassir, Gadolinia-doped ceria mixed with alkali carbonates for SOFC applications: II - An electrochemical insight, Int. J. Hydrogen Energy. 37 (2012) 19371–19379.

[28] A.I.B. Rondão, N.C.T. Martins, S.G. Patrício, F.M.B. Marques, Ionic transport in (nano)composites for fuel cells, Int. J. Hydrogen Energy. 41 (2016) 7666–7675.

[29] R.D. Shannon, Revised Effective Ionic Radii and Systematic Studies of Interatomie Distances in Halides and Chaleogenides, Acta Crystallogr. A32, (1976) 751–767.

[30] X. Guo, R. Waser, Electrical properties of the grain boundaries of oxygen ion conductors: Acceptor-doped zirconia and ceria, Prog. Mater. Sci. 51 (2006) 151–210.

[31] X. Guo, W. Sigle, J.U. Fleig, J. Maier, Role of space charge in the grain boundary blocking effect in doped zirconia, Solid State Ionics. 154–155 (2002) 555–561.

[32] Y. Lin, S. Fang, D. Su, K.S. Brinkman, F. Chen, Enhancing grain boundary ionic conductivity in mixed ionic-electronic conductors, Nat. Commun. 6 (2015) 1–9.

[33] B. Steele, Appraisal of $Ce_{1-y}Gd_yO_{2-y/2}$ electrolytes for IT-SOFC operation at 500 °C, Solid State Ionics. 129 (2000) 95–110.

[34] P.-S. Cho, S.B. Lee, Y.H. Cho, D.-Y. Kim, H.-M. Park, J.-H. Lee, Effect of CaO concentration on enhancement of grain-boundary conduction in gadolinia-doped ceria, J. Power Sources. 183 (2008) 518–523.

[35] P. Arunkumar, S. Preethi, K. Suresh Babu, Role of iron addition on grain boundary conductivity of pure and samarium doped cerium oxide, RSC Adv. 4 (2014) 44367–44376.

[36] M. Yamauchi, Y. Itagaki, H. Aono, Y. Sadaoka, Reactivity and stability of rare earth oxide–Li_2CO_3 mixtures, J. Eur. Ceram. Soc. 28 (2008) 27–34.

[37]   F.J.A. Loureiro, S. Rajesh, F.M.L. Figueiredo, F.M.B. Marques, Stability of metal oxides against Li/Na carbonates in composite electrolytes, RSC Adv. 4 (2014) 59943–59952.

[38]   S. Brosda, H.J.M. Bouwrneester, U. Guth, Electrical conductivity and thermal behavior of solid electrolytes based on alkali carbonates and sulfates, Solid State Ionics. 101 (1997) 1201–1205.

Figure and Table Captions

Figure Captions

Figure 1. A - Scheme of NLC thermal treatments: (1) NLC pellets deposited on sintered GDC; (2) NLC layer covering the pellet after melting/heat treatment; (3) Clean GDC pellet after washing with diluted HCl; B - Schemes of electrode areas (yellow/dark grey) in the in-plane (4-5) and cross (6-7) arrangements. Top views (4&6) and assumed active cell volumes (5&7, green/light shadowed regions in between electrodes).

Figure 2. Cross section views of untreated GDC (A), GDC 600 (B, C) and GDC 700 (D, E) samples. The latter images were obtained close to the surface covered by NLC (C, E) or opposite surface, nominally "NLC free" (B, D). The observed surfaces were polished and thermally etched. Dotted lines indicate the approximate disk surface positions.

Figure 3. SEM images of polished and thermally etched fracture surfaces of GDC 800 2 (top) or simply polished fracture surface of GDC 800 1 (bottom). Corresponding EDS line scan concentration profiles of Ce, Gd and Na also shown.

Figure 4. Estimated effect of distinct cell geometries and electrode configurations on impedance spectra characteristics (see text for details). The assumed equivalent circuit is shown as inset. The shaded area is often outside the available frequency range at low temperature (e.g., see Figure 6).

Figure 5. Impedance spectra in air, at 200 ºC, of GDC-based cells with surfaces untreated or treated with NLC at 600-800 ºC for 1 h (A), or at 800 ºC for different times (B). A GDCNLC3S cell is also considered for comparison (C). The inset in (A) details the Cross cell high frequency data distribution. Numbers correspond to the log of frequency (Hz).

Figure 6. Impedance spectra in air, at 200 ºC, of several GDC-based cells infiltrated with NLC at 800 ºC for 2 h. Replicas are depicted as r1 and r2. Numbers correspond to the log of frequency (Hz). Also shown data obtained with distinct a.c. signals.

Figure 7. Arrhenius-type plots of the total conductivity (A), bulk conductivity (B), grain boundary conductivity (C), and grain boundary relaxation frequency (D) of several GDC-based samples.

Figure 8. (A) Time dependence of the imposed current, at constant dc voltage of (0.5 V), across a GDC 800 2 cell. Impedance spectroscopy data obtained at 200 °C (B) and 500 °C (C) before

(open symbols) and after (filled symbols) cell polarization. Numbers correspond to the log of frequency (Hz).

Table Captions

Table 1. Sample acronyms, compositions, processing routes and electrode configurations.

Table 2. Average grain size of GDC polished and thermally etched after infiltration with NLC at distinct temperatures. Analysis performed close to the NLC covered (top) or "free" sides (bottom), see Figure 1A.

Table 3. Estimated bulk and grain boundary electrical parameters (from impedance spectra), including the stray capacitance (C_s) correction (see text for meaning of symbols).

Table 4. Electrical conductivity (σ, S.cm^{-1}) and migration energy (E_m, kJ.mol^{-1}) of tested GDC-based electrolytes.

Declaration of interests

☒ The authors declare that they have no known competing financial interests or personal relationships that could have appeared to influence the work reported in this paper.